CrossMark

Plasma emission during time-resolved laser-induced incandescence measurements of aerosolized metal nanoparticles

S. Talebi Moghaddam[1] · K. J. Daun[1]

Abstract

There has been speculation that several commonly observed anomalies in time-resolved laser-induced incandescence (TiRe-LII) measurement data may be caused by bremsstrahlung emission from a laser-induced plasma, a phenomenon known to occur at higher fluences typical of laser-induced breakdown spectroscopy. This paper presents the first theoretical framework to investigate a laser-induced plasma formation under LII measurement conditions, and explores how this plasma may affect time-resolved spectral intensity measurements. At fluences greater than 0.8 J/cm^2, the absorption cross-section of the laser-energized nanoparticle is enhanced due to inverse bremsstrahlung absorption, and bremsstrahlung emission results in an overestimation of the nanoparticle temperature due to the corruption of the incandescence signal. Under these conditions, neutral bremsstrahlung emission is more prevalent than electron–ion bremsstrahlung due to the weak nature of the induced plasma. Nevertheless, the current model does not predict laser-induced plasma phenomena below ~ 0.5 J/cm^2, typical of low-fluence TiRe-LII measurements.

1 Introduction

Nanoparticles play increasingly important roles in materials science due to their customizable electromagnetic, chemical, and transport properties, which depend strongly on nanoparticle size and shape, and can differ significantly from those of the bulk materials. Large-scale nanoparticle production often takes place in gas-phase reactors and, consequently, there is a growing demand for reliable and robust in situ diagnostics to control nanoparticle production [1, 2]. At the same time, there is an emerging awareness of the adverse effects that nanoparticles have on both human health [3] and the environment [4], which also presents a need for measuring aerosolized nanoparticles.

Time-resolved laser-induced incandescence (TiRe-LII) can be used to identify both the size and volume fraction of aerosolized nanoparticles [5–7]. In this procedure, a laser pulse heats the nanoparticles in a sample volume of aerosol, and the resulting spectral intensity is measured as the nanoparticles return to the ambient gas temperature. The spectral intensity data are connected to the unknown nanoparticle volume fraction and size distribution via two coupled submodels: the spectroscopic submodel, which relates the observed spectral incandescence with an instantaneous temperature of the nanoparticle ensemble; and the heat transfer submodel that relates the temperature decay to the nanoparticle size distribution and other attributes.

Initially, TiRe-LII was developed to determine the primary particle size and volume fraction of soot [8, 9], and has matured into a reliable mainstay combustion diagnostic. Increasingly, however, this technique is applied to measure non-carbonaceous nanoparticles, including metal [2, 10–17] and metal oxides [18, 19]. In all these scenarios, obtaining robust volume fraction and size estimates from TiRe-LII data relies on the accuracy of the measurement model. Unfortunately, candidate LII measurement models presented in the literature (including those summarized in Ref. [20]) are unable to explain several commonly observed phenomena in the experimental data, including: (1) "anomalous cooling", particularly pronounced in LII measurements on low-temperature aerosols, in which the nanoparticles appear to cool faster than can be explained via the conduction and sublimation/evaporation submodels [11, 21, 22]; (2) a higher absorption cross-section of some metallic nanoparticles at the laser wavelength compared to Mie/Drude predictions [11]; and (3) a temporary augmentation of extinction during

✉ S. Talebi Moghaddam
  stalebim@uwaterloo.ca

1 Department of Mechanical and Mechatronics Engineering,
   University of Waterloo, 200 University Ave. West, Waterloo,
   ON N2L 3G1, Canada

and shortly after the laser pulse as a function of laser fluence in combined LII/line-of-sight-absorption (LOSA) measurements [23]. Most of these phenomena have been observed over a wide range of fluences, typically starting at around 0.1 J/cm^2.

A laser-induced aerosol plasma could potentially explain each of these observations. Anomalous cooling may be due to corruption of spectral incandescence by bremsstrahlung emission, which would be most pronounced at short wavelengths, leading to an elevated pyrometric temperature lasting until the plasma dissipates [10, 21]. Enhanced absorption of the laser pulse by metal nanoparticles could be caused by inverse bremsstrahlung absorption, which may also explain the increased extinction of the aerosol during and shortly after the laser pulse in LII/LOSA measurements. Also, while Saffaripour et al. [23] speculated that the change in extinction they observed in their combined LII/LOSA measurements on soot could be due to a change in the optical properties of soot induced by laser heating, these results could alternatively be explained (at least in part) by plasma absorption. Laser-induced plasmas surrounding nanoparticles have been observed in other scenarios, albeit at higher fluences. For example, when carrying out laser-induced breakdown spectroscopy (LIBS) measurements on metal oxide nanoaerosols, Tse's group [24, 25] discovered a fluence regime, typically ~ 3 J/cm^2, in which it is possible to break down the nanoparticle and not the enveloping gas, based on the presence of atomic line emission from the nanoparticle constituents and the absence of lines from the gas constituents. They hypothesize that the laser pulse induces a localized plasma that envelops and consumes the nanoparticle, without affecting the gas. Evidence for plasma formation at even lower fluences (~ 1 J/cm^2) is provided by Menser et al. [26], who observed spontaneous atomic emission from laser-heated silicon nanoparticles, lasting for hundreds of nanoseconds after the laser pulse. This signal comes from a sustained source of excited silicon atoms, which implies the existence of laser-induced plasma. In another study, Maffi et al. [19] investigated laser-induced emission (LIE) from titania (TiO$_2$) aerosolized nanoparticles using a fluence of 0.6 J/cm^2. Their results indicated that in many cases, the radiation could not be purely presumed as incandescence and the perturbations in the signal caused by short-lived photoluminescence of titania and emission of molecular bands should be considered as incandescence signal contaminators.

The current work examines the physical phenomena that may underlie laser-induced plasma formation in LII experiments on metallic nanoparticles, and quantifies how it may affect spectral intensity measurements. Metal nanoparticles are chosen due to their importance in materials science, and because their thermophysical properties are better known than those of soot. Specifically, we examine Si (which is metallic in the liquid state), Fe, and Mo nanoparticles in argon, inspired by recent LII experiments on these types of aerosols [11, 13, 14]. The different thermophysical properties of these nanoparticles, especially the boiling point, latent heat of vaporization, and refractive index, enable a comparative analysis that provides insight into the physics underlying this phenomenon. The results show that plasma formation depends strongly on the laser pulse fluence, nanoparticle material and size, and ambient gas conditions. While plasma absorption and emission could explain both anomalous cooling and excessive absorption phenomena for high-fluence LII experiments, the current model is unable to justify some of the discrepancies reported in the literature for low-fluence experiments. Suggestions to improve the current plasma model are proposed as future work.

2 TiRe-LII measurement models

For an aerosol containing polydisperse nanoparticle sizes, the spectral incandescence intensity, $J_{\text{incand},\lambda}$, is modeled as

$$J_{\text{incand},\lambda}(t) = C_{\text{exp}}n_p \int_0^\infty p(d_p)\frac{\pi d_p^2}{4}Q_{\text{abs},\lambda}(d_p,\mathbf{m})I_{b,\lambda}\left[T_p(t,d_p)\right]d(d_p),$$

(1)

where C_{exp} is the experimental constant that accounts for the probe volume geometry, n_p is the nanoparticle number density, $I_{b,\lambda}$ is blackbody radiation intensity at the nanoparticle temperature T_p, d_p is the instantaneous nanoparticle diameter, $\mathbf{m}$ is the complex refractive index of the bulk nanoparticle material, λ is the wavelength, and $p(d_p)$ is the nanoparticle size distribution. The nanoparticle volume fraction in this work is taken to be $f_V = 2$ ppm, and the corresponding nanoparticle number density is found from $n_p = 6f_V/\pi d_p^3$. If the nanoparticle sizes are approximated as monodisperse, Eq. (1) simplifies to

$$J_{\text{incand},\lambda}(t) = C_{\text{exp}}n_p\frac{\pi d_p^2}{4}Q_{\text{abs},\lambda}(d_p,\mathbf{m})I_{b,\lambda}\left[T_p(t,d_p)\right].$$

(2)

While one may be tempted to model $Q_{\text{abs},\lambda}$ using the Rayleigh approximation since the nanoparticle sizes (~ 10–100 nm) are usually smaller than the detection wavelengths (400–800 nm), for metallic nanoparticles the requirement that the phase-shift parameter, $2\pi d_p|\mathbf{m}-1|/\lambda$, be much less than unity is usually not satisfied, so $Q_{\text{abs},\lambda}$ must be calculated using Lorentz–Mie theory [28]. The optical properties of metals can sometimes be described by the Drude model [28], or from ellipsometry measurements carried out on bulk samples.

Equation (2) connects the observed spectral intensity to the nanoparticle temperature, which is found by solving [5]

$$\frac{\pi}{6}d_{\mathrm{p}}^3\rho_{\mathrm{p}}c_{\mathrm{p}}\frac{\mathrm{d}T_{\mathrm{p}}}{\mathrm{d}t} = F_0 f(t)\frac{\pi d_{\mathrm{p}}^2}{4}Q_{\mathrm{abs},\lambda} - q_{\mathrm{evap}}\left[T_{\mathrm{p}}(t)\right] - q_{\mathrm{cond}}\left[T_{\mathrm{p}}(t)\right] - q_{\mathrm{rad}}\left[T_{\mathrm{p}}(t)\right],\tag{3}$$

where ρ_{p} and c_{p} are the density and specific heat of the nanoparticle, respectively, F_0 the laser fluence, $f(t)$ is the laser temporal profile, and q_{evap}, q_{cond}, and q_{rad} are the evaporation, conduction, and radiation heat transfer rates, respectively. In Eq. (3) $Q_{\mathrm{abs},\lambda}$ is the spectral absorption cross-section evaluated at the laser wavelength. In most TiRe-LII experiments evaporation and conduction heat transfer rates are at least several orders-of-magnitude larger than radiative cooling, and thus radiation is normally excluded from Eq. (3) [5]. Moreover, this study is focused on nanoparticles that undergo considerable evaporation during laser heating and measurement times during and shortly after the laser pulse, and, since $q_{\mathrm{evap}} \gg q_{\mathrm{cond}}$ under these circumstances, conductive cooling is also excluded from this analysis.

Evaporation also affects the mass and diameter of the nanoparticle through

$$\frac{\mathrm{d}m_{\mathrm{p}}}{\mathrm{d}t} = -m_{\mathrm{v}}\frac{q_{\mathrm{evap}}}{\Delta H_{\mathrm{v}}},\tag{4}$$

where m_{v} is the molecular mass of the evaporated species and ΔH_{v} is the latent heat of vaporization. The time-varying nanoparticle diameter is then

$$d_{\mathrm{p}}(t) = \left\{\frac{6m_{\mathrm{p}}(t)}{\pi\rho_{\mathrm{p}}(t)T_{\mathrm{p}}(t)}\right\}^{\frac{1}{3}}.\tag{5}$$

Because the diameters of the nanoparticles involved in LII measurements are smaller than the mean free path of the bath gas (> 1 μm), evaporation occurs in the free-molecular (Knudsen) regime [14]

$$q_{\mathrm{evap}} = \pi d_{\mathrm{p}}^2 N_{\mathrm{v}}'' \Delta H_{\mathrm{v}} = \pi d_{\mathrm{p}}^2 \frac{n_{\mathrm{v}}v_{\mathrm{th}}}{4}\Delta H_{\mathrm{v}},\tag{6}$$

where N_{v}'' is the number flux of evaporated molecules from nanoparticle surface,

$$N_{\mathrm{v}}''(t) = \frac{n_{\mathrm{v}}v_{\mathrm{v}}}{4} = \frac{1}{4}\underbrace{\frac{p_{\mathrm{v}}}{k_{\mathrm{B}}T_{\mathrm{p}}}}_{n_{\mathrm{v}}}\underbrace{\left[\frac{8k_{\mathrm{B}}T_{\mathrm{p}}}{\pi m_{\mathrm{v}}}\right]^{1/2}}_{v_{\mathrm{v}}}\tag{7}$$

and n_{v} and v_{v} are the number density (in molecules/m^3) and mean thermal speed of the evaporated species, p_{v} is the vapor partial pressure of the evaporated species, k_{B} is Boltzmann's constant, and m_{v} is the molecule mass of the evaporated species. In Eq. (7), p_{v}, is estimated from the Clausius–Clapeyron equation

$$p_v = p^* \exp\left[\frac{\Delta H_v(T_p - T^*)}{RT_pT^*}\right],\tag{8}$$

where p^* and T^* are the reference pressure and temperature, respectively, and R is the universal gas constant [29, 30].

3 Initial electron generation mechanisms

Plasma formation starts from a small number of "trigger electrons", which accelerate in the presence of the oscillating E–M wave and produce more electrons through impact ionization, thereby initiating an "electron cascade". Trigger electrons can potentially arise from two primary candidate sources for an aerosol: (1) the molecules in the gas phase surrounding the nanoparticle, including both evaporated nanoparticle molecules and bath gas molecules; and (2) the metallic nanoparticle itself. The interaction of the laser pulse with the gas-phase molecules can release initial electrons due to multiphoton ionization (MPI), while electrons can be emitted by the nanoparticle through plasmonic decay photoemission [31], thermionic emission [32], and thermally-assisted photoemission [33]. We consider the plausibility of each scenario below.

3.1 Trigger electrons from the gas-phase

A molecule having an ionization potential of J_{ion} can be directly ionized by a photon having a larger energy $e_{\mathrm{p}} = h\nu$. However, several photons with energies below the atomic ionization potential can also ionize the molecule via MPI if they interact with the molecule in a timescale shorter than the relaxation time of the valence electron. The ionization rates for both the evaporated species and bath gas molecules are proportional to $I^{n_{\mathrm{ph}}}$ [34]

$$W_{\mathrm{MPI}} = \sigma_{\mathrm{MPI}}(\lambda, J_{\mathrm{ion}})I^{n_{\mathrm{ph}}},\tag{9}$$

where I is the pulse intensity, σ_{MPI} is the MPI cross-section of each species, and n_{ph} is the number of photons simultaneously required to ionize each species,

$$n_{\mathrm{ph}} = \mathrm{int}\left(\frac{J_{\mathrm{ion}}}{e_{\mathrm{p}}} + 1\right) = \mathrm{int}\left(\frac{J_{\mathrm{ion}}}{h\nu} + 1\right).\tag{10}$$

While MPI is a viable source of trigger electrons in LIBS experiments carried out at higher fluences [35], the

laser intensities and pulse durations typical of LII experiments are insufficient to ionize the metal vapors. Moreover, experiments on bulk silicon irradiated by a 1064-nm laser pulse with intensities up to 10^7 W/cm^2, far higher than those typical of LII measurements, showed no evidence of MPI-generated electrons [36], and, since the ionization energy of the bath gas molecules exceed those of evaporated metal atoms (e.g., Ar has a first ionization energy of 15.57 eV [37] while that of Si is 8.15 eV [38]), this result would appear to immediately disallow MPI as a candidate source of trigger electrons in LII experiments.

However, some metallic nanoparticles act as "antennas" in the presence of an oscillating *E–M* field due to plasmonic effects, which causes high-intensity near-field regions to form in the vicinity of the nanoparticle [39, 40]. In such cases, a molecule located within the near-field region may encounter a much higher intensity field compared to one that is further away. This phenomenon has been exploited to reduce the fluence threshold needed to produce a laser-induced plasma surrounding gold nanoparticles in water [41, 42]. The near-field electric/magnetic spatial intensity profile is given by $n_{NF}(\mathbf{r}) = E(\mathbf{r})/E_0$, where E_0 is the incident-field electrical intensity, and $E(\mathbf{r})$ is the electric field in the vicinity of the nanoparticle. This quantity can be readily found using Mie theory [41, 43, 44] for isolated nanospheres. Figure 1a shows $n_{NF}(\mathbf{r})$ contours for a 30-nm liquid silicon nanoparticle, and maximum field enhancements for Fe, Mo, Si and Ag nanoparticles are plotted in Fig. 1b as a function of nanoparticle size. Incorporating these near-field enhancements into Eq. (9), using pulses up to 5 J/cm^2 with a 10-ns top-hat pulse ($I < 5 \times 10^8$ W/cm^2), and assuming that evaporated atoms remain within the enhanced region during the entire laser pulse duration resulted in an insignificant amount of MPI ionization. Therefore, MPI ionization can be discounted as a candidate source of trigger electrons in 1064 nm LII experiments for Fe, Mo, Ag, and Si nanoparticles. This conclusion may not hold at a shorter excitation wavelength, for example, 532 nm, due to the higher photon energy.

3.2 Trigger electrons from the nanoparticle

Electron emission from the nanoparticle may also be enhanced through plasmonics. Following plasmon excitation due to light absorption, electromagnetic decay occurs on a femtosecond time scale, either radiatively through photon re-emission or non-radiatively by emitting hot electrons [45]. In the non-radiative process, surface plasmons first decay into single-electron excited states. This may be followed by photoemission if the electron exceeds the work function of the material, which specifies the energy needed for an electron to escape the metallic surface. Electron emission may originate from the conduction band, and, in the case of noble plasmonic metals, the valence bands (e.g., d-band) [46–48]. Plasmonic decay has been used extensively for enhancing the efficiency of photovoltaics using noble metals nanoparticles such as Au and Ag [49–51]. However, our analysis of Fe, Mo and Si nanoparticles between 10 and 100 nm, irradiated by 1064 nm pulse, did not exhibit any plasmonic decay photoemission. Nevertheless, this phenomenon could be a contributing factor for trigger electron emission in LII experiments on Ag nanoparticles (e.g., Refs. [11, 52]), which is an ongoing field of investigation.

Thermionic emission [32] represents another candidate source of trigger electrons from the nanoparticle. It arises from the fact that electron energies within a metal obey a Boltzmann distribution, and a fraction will thus have an energy exceeding the work function. The rate of electron emission J_{th} is governed by the Richardson–Dushman equation [32]

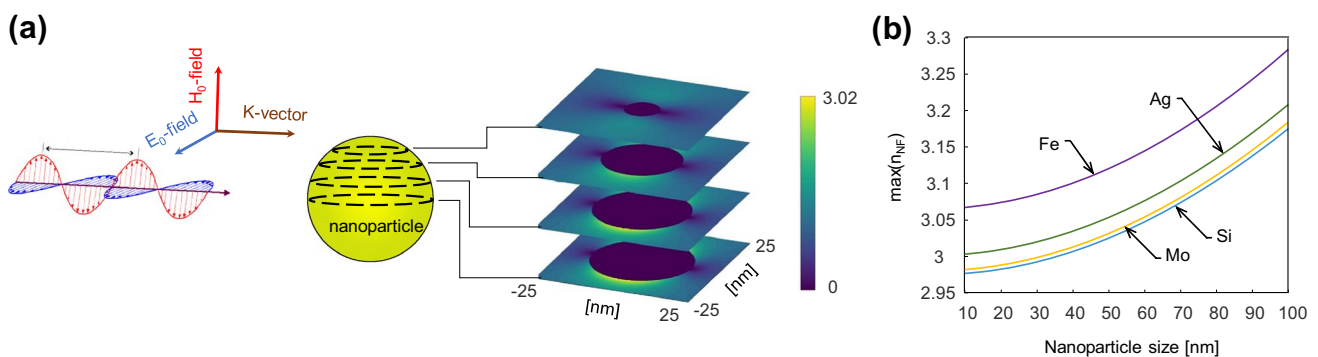$$J_{th} = A T_p^{\,2} \exp\left[\frac{-W - \Phi_e}{k_B T_p}\right], \tag{11}$$

Fig. 1 **a** Near-field enhancement around a 30-nm silicon nanoparticle interacting with 1064-nm incident wavelength. **b** Maximum near-field profile as a function of nanoparticle size for different nanoparticles

where $A = 7.503 \times 10^6$ electrons/(nm^2 s K^2), W is the work function, and k_B is Boltzmann constant. The ionization potential, Φ_e, depends on the spontaneous charge of the nanoparticle N_e and its size according to [53]

$$\Phi_e(t) = \frac{N_e^2(t)e^2}{4\pi\varepsilon_0 d_p(t)} \, \text{sgn}(N_e), \tag{12}$$

where ε_0 is the vacuum permittivity and $\text{sgn}(N_e)$ is the sign of the nanoparticle accumulated charge. Thermionic emission has been included in some LII models, but only in the context of how it affects nanoparticle cooling [54, 55].

The number flux of ionized atoms evaporated from the nanoparticle surface can be found from the Saha–Langmuir equation, which is derived assuming local thermal equilibrium across the phase interface of the nanoparticle [32]. The ratio of the number density of evaporated ionized species n_1 to neutrals n_0 is

$$\frac{n_1}{n_0} = \frac{Z_1}{Z_0} \exp\left[\frac{-W_i + W + \Phi_e}{k_B T_p}\right], \tag{13}$$

where Z_1 and Z_0 are associated partition functions. In the case of silicon nanoparticles at 4000 K (a typical peak LII temperature) these are 5.6 and 9.1, respectively [56], and W_i is the ionization potential. Ion emission will change the ionization potential, Φ_e, and consequently augment the electron emission rate, J_{th}.

The accumulated number of electrons emitted by the nanoparticle is limited by ionization potential growth due to positive charge build-up of the nanoparticle, cf. Equation (12). As an example, Mitrani et al. [55] predicted that approximately 25 accumulative electrons would be emitted from a 32-nm-diameter graphite nanoparticle during an LII

measurement, which would likely be inadequate to initiate a plasma. However, most metallic nanoparticles have significantly higher evaporation rates compared to carbonaceous nanoparticles, resulting in more ion emission via the Saha–Langmuir equation. Ion emission reduces the positive charge potential and induces more electron emission from the nanoparticle. This assumption is valid for the case of a low ion density accumulation in the vicinity of the nanoparticle so that the emission of ions does not affect the Richardson–Dushman equation [32]. The emission of thermal electrons strongly depends on the rate of atom and ion evaporation, which, in turn, depends on absorption efficiency of the nanoparticle as well as the enthalpy of vaporization and atomic mass.

Accumulative thermionic electron emission from a 40-nm-diameter Si nanoparticle is shown in Fig. 2a for different fluences. The accumulative electron emission increases at high fluences due to higher temperatures and evaporation rates, which collectively result in a greater rate of ion emission from the nanoparticle. Also, the ratio of the total number of emitted ions to the total emitted molecules (taken to be single Si atoms [57]) is less than 2.5% as shown in Fig. 2a. If the effect of ion emission on the nanoparticle charge state is neglected, on the other hand, only 12 electrons are emitted. Low electron emission, in this case, is due to the positive charge built-up that halts the emission of thermal electrons early during the pulse, as shown in Fig. 2b. This analysis suggests that, for low melting-point metals, thermionic emission is the most likely candidate source of trigger electrons.

Finally, thermally assisted multiphoton photoelectric emission [33, 58, 59] arises from the fact that the work function drops by increasing the plasmon electron energy over the Fermi level due to the elevated temperature of the
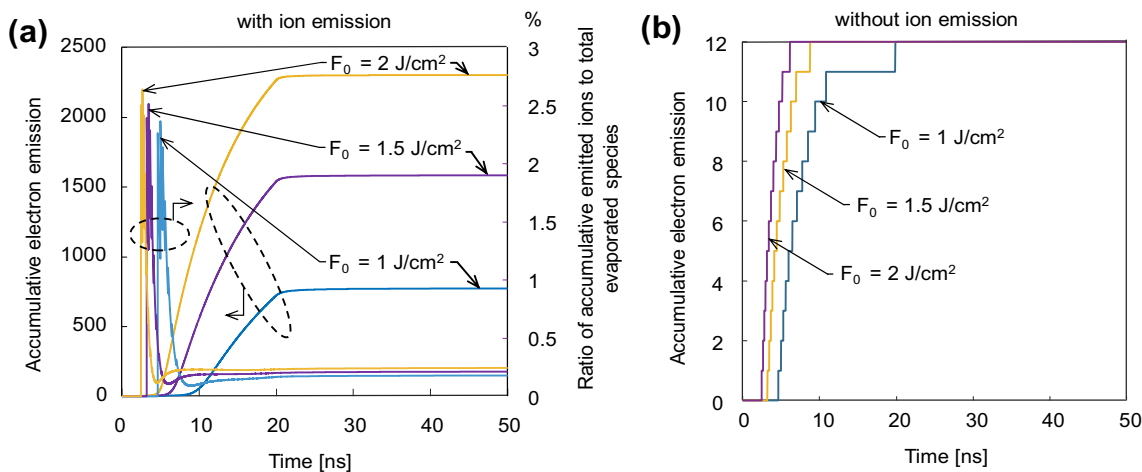

Fig. 2 Accumulative electron emission, and ratio of emitted ions to total evaporated species, from a Si nanoparticle during a 20-ns top-hat laser pulse for three different fluences with: **a** the influence of ion emission on the charge state of the nanoparticle; and **b** neglecting this effect

material. This, in turn, increases the probability of multiphoton ionization from the nanoparticle. During a laser pulse lasting on the order of nanoseconds, one would expect electrons emitted through thermally assisted multiphoton photoelectric emission to precede thermionic emission, since the former scenario can occur at lower temperatures. Modeling this phenomenon requires several empirically-derived coefficients [60], which, to the best knowledge of the authors, are unavailable for liquid Fe, Mo, and Si. Accordingly, this phenomenon is excluded from this study.

4 Laser-induced aerosol plasma generation

A plasma forms when trigger electrons accelerate in the presence of the oscillating *E–M* field of the laser and collide with the bath gas molecules and evaporated nanoparticle neutrals and ions. The number density of neutral bath gas molecules far exceeds the evaporated nanoparticle atoms in LII experiments, so one may expect that the primary interaction between the *E–M* wave and the plasma is via inverse neutral bremsstrahlung absorption as the electrons scatter from the neutral bath gas species. Further ions and electrons are generated from the interaction of electrons with metallic evaporated molecules via impact ionization of the evaporated molecules. Some of the free electrons combine with the ions to produce neutrals.

The initial 100 ns of plasma formation and growth is called the "early plasma" problem [61]. The characteristic time constant for gas-phase collisional processes is much longer than those governing processes that control transport across the nanoparticle phase boundary. Accordingly, local thermal equilibrium (LTE), which underlies both the Saha equation, describing the ionization states of gas-phase species, and Boltzmann kinetic theory, which governs the distribution of atomic energy levels [61], is unlikely to hold. Instead, empirical relations are used to model the initial breakdown event [62]. Unfortunately, the few models reported in the literature apply to lower laser wavelengths and higher pulse intensities compared to those used in LII experiments, which result in significantly higher MPI-driven electron emission [62–64]. Therefore, we must derive empirical electron growth equations appropriate to LII experiments [65].

In order to simplify the analysis, electron and ion growth models neglect electron diffusion and

recombination. Moreover, the electron impact ionization rate is assumed to be sufficiently high to ionize all the evaporated species. The net effect of these assumptions and simplifications is to provide the maximum possible number density of electrons and ions, and thus the maximum possible influence of laser-induced plasma emission on LII measurements. We also assume that the electrons are not sufficiently energetic to ionize the LII bath gas species, which has a much higher ionization potential. This treatment is supported by the fact that typical LII fluences are less than those used in PS-LIBS [25], in which no bath gas ionization was observed. Double ionization of the evaporated species is similarly unlikely, since Si^{2+}, Fe^{2+} and Mo^{2+} ionization potentials are approximately equal to the Ar^+ ionization potential.

The duration of the LII laser pulse is usually less than 30 ns. Early plasma dynamics suggest that there is an insufficient opportunity for the plasma to equilibrate with the LII bath gas molecules [63, 66]. Therefore, it can be assumed that the electrons and ions emitted by the nanoparticle are at a much higher temperature compared to the bath gas. Accordingly, the LII plasma submodel consists of two distinct systems: (1) the bath gas, which is assumed to be in local thermal equilibrium (LTE) at T_g; (2) and ions and electrons emitted by the nanoparticle having speeds that approximately obey Maxwellian distributions corresponding to the plasma temperature T_{pl} and their respective masses.

5 Thermal emission from a laser-induced plasma

Broadband emission and absorption of a plasma is a consequence of the non-quantized ("free–free") transitions in electronic translational energy states [67]. Continuum emission originates from non-quantized deceleration of free electrons as they interact with charged particles or the atomic field of neutrals. Likewise, photons are absorbed by free electrons undergoing sudden acceleration around ions and neutrals via inverse bremsstrahlung. Accordingly, plasma emission depends on the instantaneous spatial distribution of the electrons, ions, and neutrals, as well as their temperatures.

Bremsstrahlung radiation due to scattering of electrons from ions per unit volume, time, solid angle, and wavelength is given by [68, 69]

$$E_{e-i,\lambda}(T_{pl}, \mathbf{r}, \lambda, t) = \underbrace{\frac{16}{3}\left(\frac{\pi}{6}\right)^{1/2}\frac{q_e^6}{c_0^2 m_e^2}\left(\frac{m_e}{k_B}\right)^{1/2}}_{C_{e-i}}\frac{n_e(t)n_i(r,t)}{\lambda^2 T_{pl}^{1/2}(t)}Z^2 g_{e-i}\exp\left(\frac{-hc_0}{k_B\lambda T_{pl}(t)}\right),$$

(14)

assuming a Maxwellian distribution over electron and ion velocities. The quantum–mechanical correction factor g_{e-i} (Gaunt factor) is assumed to be unity due to the low number density of ions, n_i, and electrons, n_e, and ionic charge number Z^2 is also unity due to the single ionization state. The constant C_{e-i} is related to electron mass, m_e, electron charge, q_e, Boltzmann constant, k_B, and speed of light in a vacuum, c_0. Equation (14) is averaged over the LII probe volume to account for spatial variation in the plasma temperature and density.

Neutral bremsstrahlung emission and absorption is calculated using the emission cross-section from Dalgarno and Lane [70, 71]

$$\frac{d\sigma_\nu(E)}{d\nu} = \frac{8r_e}{3c_0}\frac{E}{h\nu}\left(1-\frac{h\nu}{E}\right)^{1/2}\left[q_0(E-h\nu)+\left(1-\frac{h\nu}{E}\right)q_0(E)\right],$$
(15)

where r_e is the classical electron radius, E is the initial electron energy, $\nu=c_0/\lambda$ is the frequency, $h\nu$ is the photon energy, and q_0 is the electron momentum cross-section as a function of electron energy. Equation (15) expresses the neutral bremsstrahlung cross-section arising from electron-neutral elastic scattering in the limit of low-energy photons using the phase-shift approximation [72]. The energy radiated from neutral bremsstrahlung per unit time, unit volume, solid angle, and wavelength is then found by integrating Eq. (15) over the electron energy distribution,

$$E_{NB,\lambda}(t,T_{pl}) = \frac{n_n n_e(t)h\nu}{4\pi}\int_{h\nu}^\infty v_e(E,T_{pl})\left[\frac{d\sigma_\nu(E)}{d\nu}\frac{c_0}{\lambda^2}\right]f(E,T_{pl})dE,$$
(16)

where n_n is the number density of LII bath gas neutrals and $v_e(E)$ is the initial velocity of the electron as a function of electron energy. The c_o/λ^2 term changes the unit of neutral bremsstrahlung cross-section from frequency to wavelength, and $f(E)$ is the electron energy distribution in the gas medium. Neutral bremsstrahlung emission is calculated by numerically integrating Eq. (16) using a value of $d\sigma_\nu/d\nu$ derived from a momentum cross-section reported the literature [73], and a Maxwellian distribution over $f(E)$ at an electron temperature of T_{pl}. Finally, the total contribution of plasma emission to the detected LII signal is found by

$$J_{pl} = J_{NB,\lambda} + J_{e-i,\lambda} = C_{exp}(E_{NB,\lambda} + E_{e-i,\lambda}).$$
(17)

The plasma temperature can increase considerably during the laser pulse due to inverse bremsstrahlung heating, but this is difficult to calculate. Under near-threshold breakdown conditions, the plasma temperature is typically between 1/3 to 1/4 of the ionization potential of the ionized species [74], which corresponds to approximately $T_{pl} \sim 2$ eV, so this value is adopted unless otherwise noted.

The distribution of electrons within the probe volume is assumed to be spatially uniform due to their low mass, high

speeds, and small Coulomb attraction force between ions and electrons [65]. In contrast, the distribution of the ions is limited by their considerably slower speeds and the finite diffusion rate through the ambient enveloping gas. Based on transient Direct Simulation Monte Carlo (DSMC) simulations on the dispersion of C_3 species around a laser-heated soot aggregate [75, 76], and given the spacing of the aerosol considered here ($\sim 3.2\times 10^3$ nm for $f_v = 2$ ppm, $d_p = 50$ nm) we can assume that the clouds of evaporated species around each nanoparticle do not overlap. Therefore, the number of ions in each microplasma, N_i, is equal to the evaporated species from a single nanoparticle, while molecular diffusion governs the spatial distribution of ions, and roughly follows $1/r^2$ at any instant. The exact distribution does not matter, however; integration of Eq. (14) with any proposed ion distribution and uniform electron distribution results in

$$J_{e-i,\lambda} = c_{exp}c_{e-i}n_p^2 \frac{N_e N_i}{\lambda^2 T_{pl}^{1/2}}Z^2 \exp\left(\frac{-hc_0}{k_B\lambda T_{pl}}\right).$$
(18)

Equation (18) shows that electron–ion plasma emission depends only on the total number of emitted ions, N_i. Also, $J_{e-i,\lambda}$ depends on n_p^2, while neutral bremsstrahlung depends on n_p. Moreover, we should consider that a higher n_p value results in a higher initial electron population density and therefore a higher MPI ratio, which leads to a higher final electron population at the end of the pulse. However, in this work, we assume that the evaporated neutrals are completely ionized in the gas surrounding the nanoparticle, so this does not affect the plasma absorption or emission.

Since the evaporated species are assumed to be completely ionized, the population of neutral atoms surrounding the nanoparticle remains constant and consists exclusively of gas molecules. The evaporation rate, which defines the accumulative number density of electrons and ions, is found by solving Eqs. (3) and (4) simultaneously.

6 Results and discussion

The model described above is used to predict plasma formation and emission from laser-heated Si, Fe, and Mo nanoparticles to determine how this effect is influenced by nanoparticle size and composition, ambient temperature, and laser fluence. In all cases, the initial nanoparticle temperature is that of the bath gas, taken to be 300 K for Mo and Fe nanoparticles, following Ref. [12], and 1500 K for the Si nanoparticles, as in Ref [14]. The refractive indices and thermophysical properties of Fe and Mo are taken from Ref. [77, 78], while those of liquid Si come from Ref. [14]. While in reality, the time-averaged laser temporal profile is usually Gaussian, to simplify our analysis we instead assume a top-hat temporal profile of 10 ns duration.
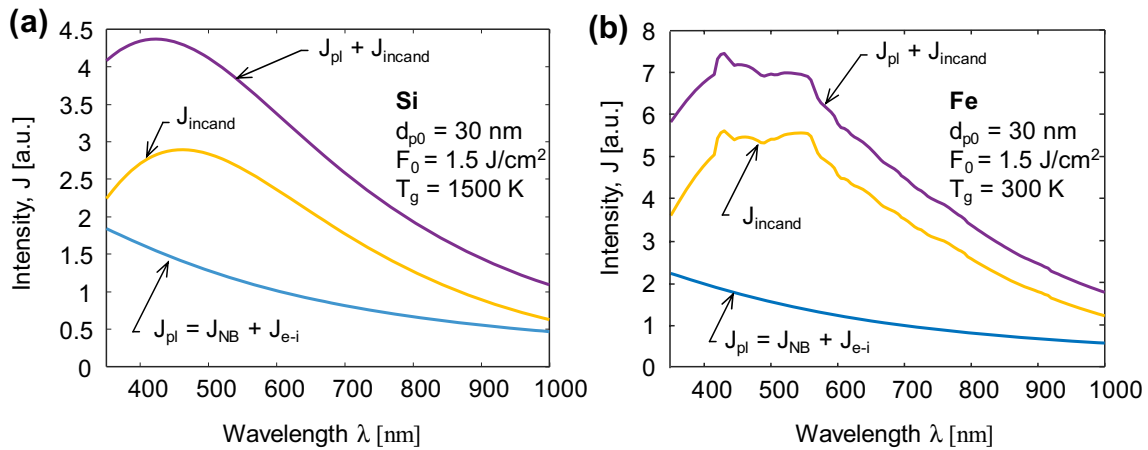
(a)

(b)

Fig. 3 Comparison of bremsstrahlung emission with nanoparticle incandescence, J_{incad}, at the peak temperature of the nanoparticle, **a** Si nanoparticle and **b** Fe nanoparticle. The non-smooth features of the Fe nanoparticle emission arise from artifacts in the ellipsometry data used to calculate the refractive index of molten iron
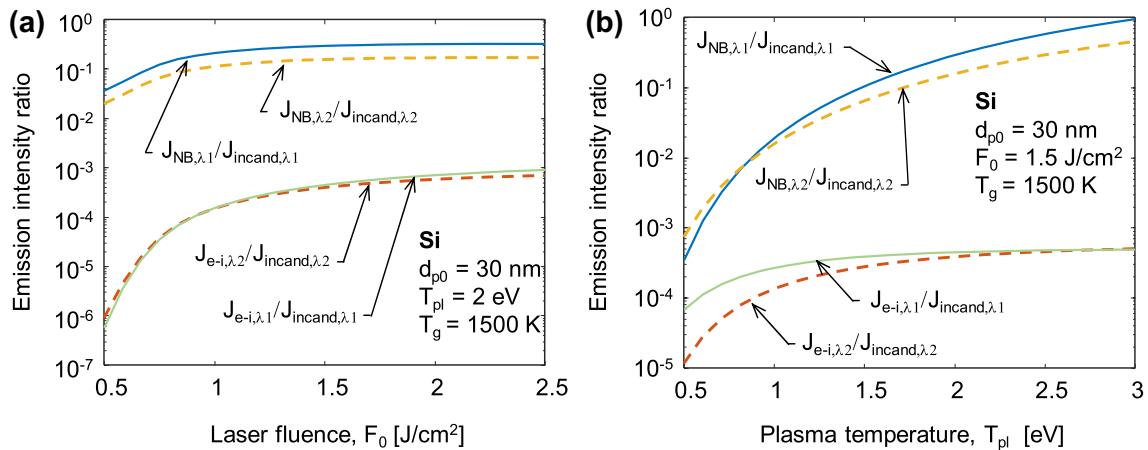
(a)

(b)

Fig. 4 Neutral bremsstrahlung, $J_{NB,\lambda}$, and electron–ion bremsstrahlung, $J_{e-i,\lambda}$, ratios to nanoparticle incandescence, $J_{incand,\lambda}$, at nanoparticle peak temperature for detection wavelengths $\lambda_1 = 442$ nm and $\lambda_2 = 716$ nm: **a** intensities as a function of laser fluence at a constant plasma temperature; **b** intensities as a function of plasma temperature at a constant laser fluence

Figure 3 shows how plasma emission corrupts the nanoparticle incandescence signal for Si and Fe nanoparticles (one would expect the radiative properties of molten iron to be a smooth function of wavelength, and the spectral features are likely artifacts of the ellipsometry technique used to derive **m** [77]). Note that the plasma emission is "blue shifted" compared to the incandescence signal, and, consequently, the bremsstrahlung-contaminated incandescence signal has a peak at a wavelength shorter than the incandescence signal by itself.

Figure 4a, b shows that neutral bremsstrahlung emission is an order-of-magnitude larger than electron–ion bremsstrahlung for all electron temperatures and laser fluences. This is due to the high density of neutral LII bath gas atoms compared to electrons and ions, which is consistent with experiments on weak plasmas [79, 80]. Electron–ion bremsstrahlung emission is related to the number density of electrons and ions by Eq. (14), and is independent of the bath gas type and number density. In contrast, neutral bremsstrahlung emission depends on the number density of electrons and neutrals in the gas-phase. Therefore, both the pressure and temperature of the bath gas strongly influence neutral bremsstrahlung emission.

To assess how plasma emission affects the inferred nanoparticle temperatures, pyrometry is carried out on the modeled spectral intensity, erroneously assuming that the detected signal is purely incandescence at $\lambda_1 = 442$ nm and $\lambda_2 = 716$ nm. Initially, we calculate the pyrometric temperature through nonlinear least-squares regression of the incandescence model at two wavelengths to the corresponding spectral intensities
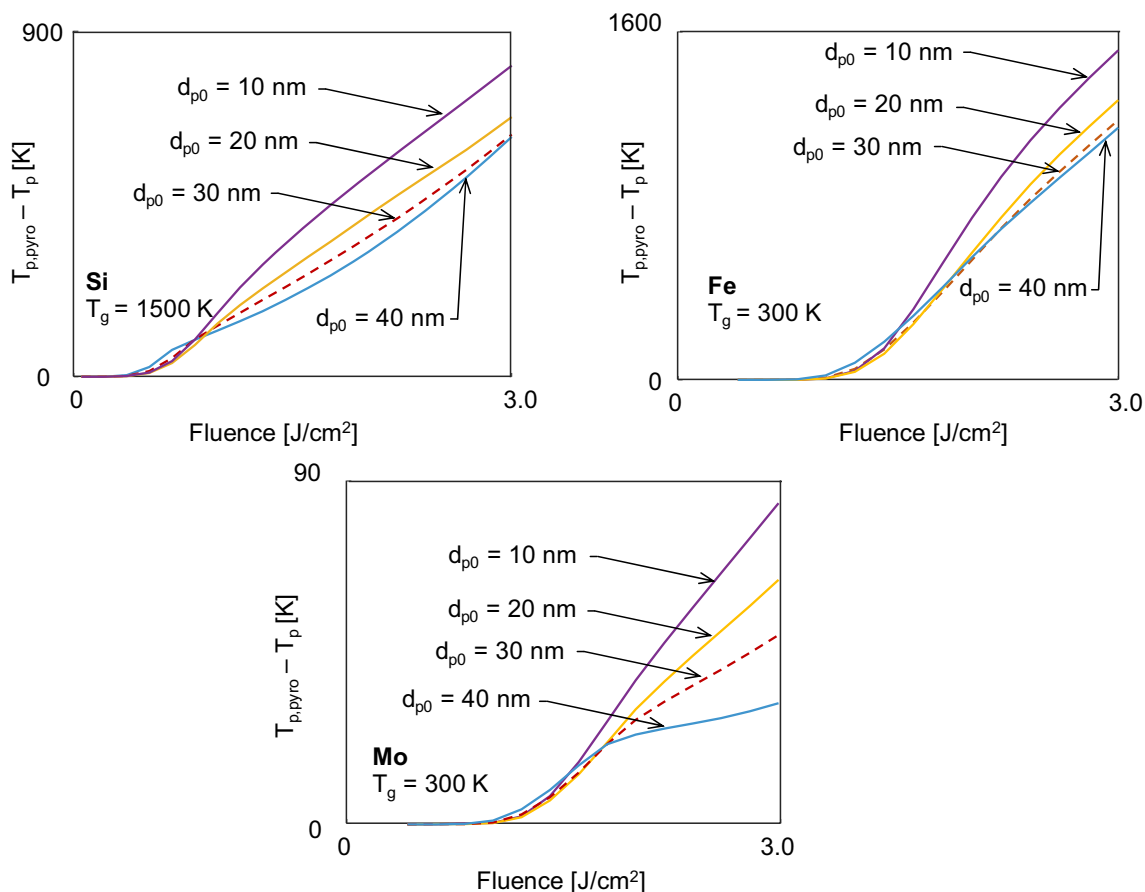
Fig. 5 Neutral bremsstrahlung, $J_{NB,\lambda}$, and electron–ion bremsstrahlung, $J_{e-i,\lambda}$, ratios to nanoparticle incandescence, $J_{incand,\lambda}$, at nanopaticle peak temperature for detection wavelengths $\lambda_1 = 442$ nm and $\lambda_2 = 716$ nm as a function of nanoparticle loading
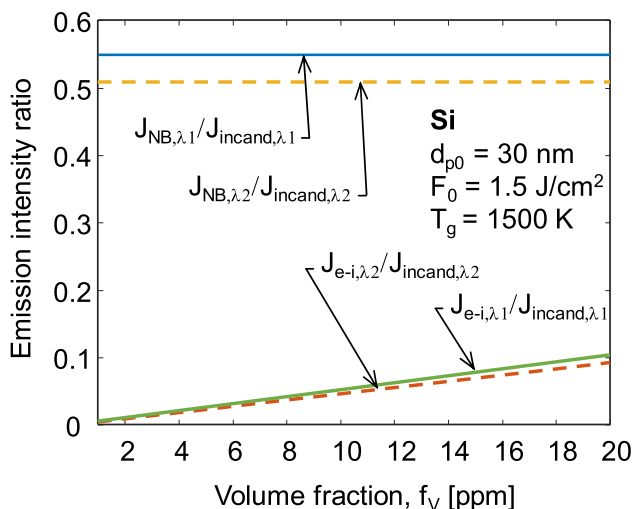

Fig. 6 Difference between real and pyrometrically inferred peak temperatures for different nanoparticle materials. In the analysis, particle loading is 2 ppm, $T_{pl} = 2$ eV, $P_g = 101$ kPa

calculated using the incandescence + plasma model. In all cases, the maximum error increases with fluence due to increased evaporation, although, as one may expect, the influence of the plasma on the pyrometric temperature depends strongly on the nanoparticle type, initial diameter, d_{p0}, and laser fluence, cf. Fig. 5. The peak temperature error for the Mo nanoparticles is lower than the others due to its higher boiling point and lower evaporation rate. In general, the error is most significant for the smallest nanoparticles, since the ratio of the plasma and nanoparticle absorption cross-sections is largest. If one uses Wien's approximation to carry out ratio pyrometry, the error is generally less, and varies strongly with the material. This effect could, in some circumstances, explain anomalous cooling, since one would expect the pyrometry error to drop as the plasma dissipates over time, but confirmation of this effect requires a detailed transport model for the plasma species.

Due to the dominance of neutral bremsstrahlung over electron–ion bremsstrahlung, the linear relationship between neutral bremsstrahlung emission and electron density in Eq. (16), and the fact that the neutral density n_N remains
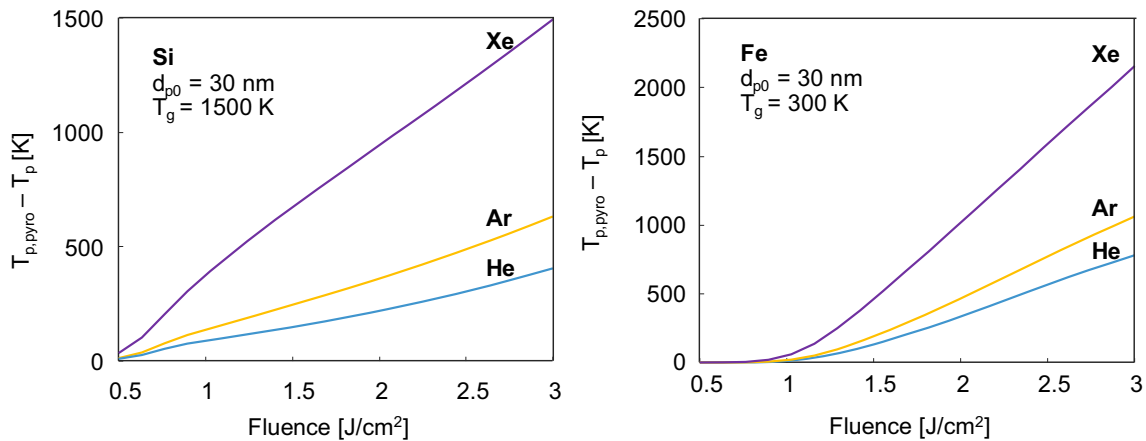
Fig. 7 Difference between real and pyrometrically inferred peak temperatures for different nanoparticle materials with different LII bath gas species. In the analysis, particle loading is 2 ppm, $T_{pl} = 2$ eV, $P_g = 101$ kPa

constant, the pyrometry error is independent of the nanoparticle loading since it scales both incandescence and neutral bremsstrahlung emissions in the same way, as shown in Fig. 6. However, the electron–ion bremsstrahlung ratio increases with the particle loading.

The electron momentum cross-section q_0 in Eq. (15) is largest for molecules having high polarizability [79]. Therefore, we expect to see a more substantial pyrometry error for experiments with LII bath gas species having higher polarizabilities, cf. Fig. 7. Although the LII bath gas species type influences the nanoparticle cooling rate through conduction heat transfer, the peak nanoparticle temperature is determined by a balance between the energy added by the laser and the energy lost due to evaporation, which are both independent of the bath gas. Therefore, a change in the peak temperature for different LII bath gas species indicates neutral bremsstrahlung emission.

Figure 8a, b shows that the pyrometrically inferred peak temperature error for an iron nanoparticle is sensitive to both bath gas pressure and temperature. The peak temperature error increases approximately linearly with increasing bath gas pressure, which is proportional to n_N. The relationship with gas temperature is more complex: the error initially decreases with increasing bath gas temperature, since $n_N \propto 1/T_g$, but increases at higher temperatures, since higher bath gas temperatures lead to higher nanoparticle peak temperatures and greater evaporation rates for a given fluence.

The plasma also absorbs the laser pulse through inverse-bremsstrahlung, through a combination of neutral and electron–ion interactions. The ratio of the IB absorption efficiency, Q_{pl}, at 1064 nm, and the nanoparticle absorption efficiency calculated using Mie theory, Q_{NP}, is shown in Fig. 9 as a function of fluence. The plasma cross-section is less than the nanoparticle cross-section up to 3 J/cm², at which point Q_{pl} begins to
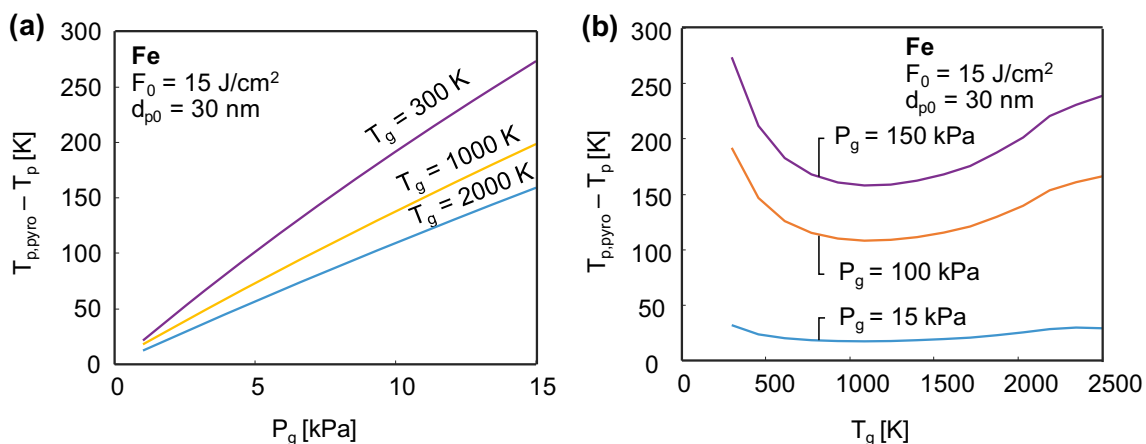

Fig. 8 **a** Peak temperature inference error due to bremsstrahlung emission as a function of LII bath gas pressure. **b** Peak temperature inference error as a function of LII bath gas temperature
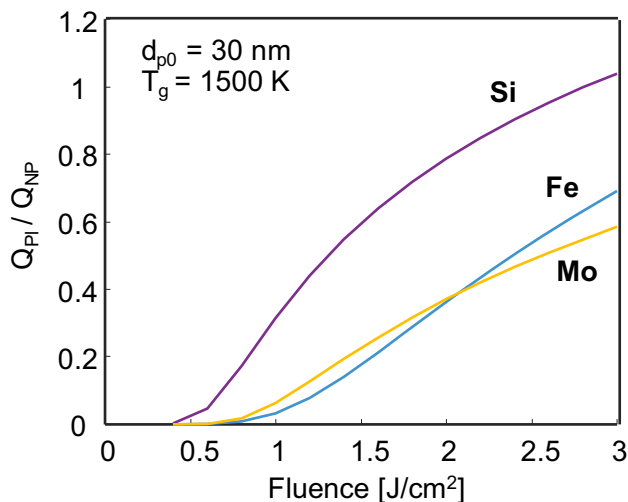
Fig. 9 Absorption of the nanoparticle (Q_{NP}) compared with the absorption of the plasma (Q_{Pl}) for different nanoparticle materials at $\lambda = 1064$ nm

dominate the absorption cross-section. This is for two reasons: first, the physical cross-section of the nanoparticle drops at higher fluences due to evaporation; and second, the evaporated species ionizes and generates a higher-density plasma. Therefore, Q_{pl}/Q_{NP} is expected to be larger for higher fluences, and also for shorter pulses. This effect is most significant for highly conducting metallic nanoparticles, which have a low nanoparticle absorption cross-section. As a specific example, Ag nanoparticles at 1064 nm have an even lower absorption cross-section compared to the metallic nanoparticles considered in this study [11], and one would expect the neutral bremsstrahlung cross-section, calculated from Eq. (16), to dominate nanoparticle incandescence. This may be the explanation for the fact that, in their LII measurements of Ag nanoparticles, Sipkens et al. [11] reported peak temperatures around 2800 K, which is much higher than the Ag boiling temperature of 2130 K. Were this temperature to reflect the true peak nanoparticle temperature, the nanoparticle absorption cross-section would need to be at least 16 times higher compared to the one predicted by Mie–Drude theory in order to absorb enough laser energy. Accordingly, we also do not expect to induce a plasma in the system. On the other hand, any electron emission from the nanoparticle still can emit neutral bremsstrahlung, which may be the source of the observed radiation.

Finally, it should be remarked that the fluence range in which neutral bremsstrahlung is comparable in magnitude with the incandescence, cf. Fig. 4, is higher than the fluence range at which many of the unexplained LII phenomena described in the introduction occur. Excessive absorption in the LII experiments has been observed over 0.1–0.5 J/cm^2 [11, 16], while anomalous cooling usually occurs between 0.1 and 0.3 J/cm^2 [11, 21, 81, 82]. The exception is the

unexplained secondary Si atomic emission lines observed by Menser et al. at fluences above 1 J/cm^2 [26], which is consistent with the fluence range considered in this study. The secondary lines are distinct from the primary lines that coincide with the laser pulse, and are attributed to evaporation of thermally-excited Si atoms. The secondary lines have their peak about 200 ns after the peak laser fluence, and the total length of the signal is about 700 ns. This timescale points to a gas-phase collisional process (possibly electron/neutral recombination) as a source of excited Si atoms, which fluoresce as they relax. The plasma predicted by the proposed model may, in turn, be the source of the electrons.

7 Conclusions

There has been speculation that some commonly observed and as-yet unexplained LII phenomena may be caused by a laser-induced plasma linked to nanoparticle evaporation. This study is a first attempt to define a theoretical basis for plasma formation around a metallic nanoparticle during laser-induced incandescence. We examined several candidate sources for the trigger-electrons needed to initiate the plasma cascade, and found that, for excitation wavelengths of 1064 nm, thermionic emission remains the most probable source, due to the influence of ion evaporation on the nanoparticle charge state. The cascade then occurs through electron impact ionization of evaporated species into a singly ionized state. The plasma model presented in this paper shows that, under normal LII conditions, neutral bremsstrahlung dominates over electron–ion bremsstrahlung due to the low number densities of electrons and ions.

Broadband plasma emission contaminates the background incandescence from the nanoparticle at fluences greater than 1 J/cm^2, and is most pronounced for metallic nanoparticles having a low melting point, due to the enhancement of thermionically-emitted electrons, and lowers the spectral absorption cross-section of the nanoparticle, which leads to a weak background incandescent emission. Since plasma emission is most pronounced at short wavelengths, contamination of the LII signal leads to overestimation of the nanoparticle temperature. Inverse bremsstrahlung absorption may also explain the enhanced absorption cross-section observed in LII measurements on metal nanoparticles and, potentially, the increased extinction observed in combined LII/LOSA studies.

While the present analysis suggests that the formation of laser-induced plasmas is unlikely in low-fluence LII experiments, it is important to note that many of the phenomena observed by LII practitioners appear to be consistent with the bremsstrahlung-contaminated incandescence signals predicted at higher fluences. Anomalous cooling, for example, is more pronounced in LII experiments carried

out on aerosols at ambient temperatures and pressures, which is consistent with the model predictions. It may be that the simplifications needed to derive the plasma model (e.g., uniform electron density) do not capture key mechanisms underlying plasma formation, although neglecting electron diffusion and recombination, and assuming total ionization of the evaporated species likely overestimate the possibility of plasma formation and not the other way around. It may also be that the unexplained LII phenomena may originate from electron/neutral bremsstrahlung, but without the electron cascade/impact ionization associated with plasma formation. For example, preliminary calculations show that bremsstrahlung caused by plasmonically enhanced electron emission and the neutral gas species could account for the detected LII signal from silver nanoparticles. Further theoretical and experimental analyses, including comparative LII measurements on a range of aerosols and over a broad set of wavelengths, are needed to understand this phenomenon.

References

1. T. Dreier, C. Schulz, Laser-based diagnostics in the gas-phase synthesis of inorganic nanoparticles. Powder Technol. **287**, 226–238 (2016). https://doi.org/10.1016/j.powtec.2015.10.015

2. K. Daun, J. Menser, R. Mansmann, S.T. Moghaddam, T. Dreier, C. Schulz, Spectroscopic models for laser-heated silicon and copper nanoparticles. J. Quant. Spectrosc. Radiat. Transf. **197**, 3–11 (2017). https://doi.org/10.1016/j.jqsrt.2016.10.006

3. S.K. Sahoo, S. Parveen, J.J. Panda, The present and future of nanotechnology in human health care. Nanomedicine **3**, 20–31 (2007). https://doi.org/10.1016/j.nano.2006.11.008

4. D.T.L. Alexander, P.A. Crozier, J.R. Anderson, Brown carbon spheres in east Asian outflow and their optical properties. Science (80–) **321**, 833–836 (2008). https://doi.org/10.1126/science.1155296

5. H.A. Michelsen, C. Schulz, G.J. Smallwood, S. Will, Laser-induced incandescence: particulate diagnostics for combustion, atmospheric, and industrial applications. Prog. Energy Combust. Sci. **51**, 2–48 (2015). https://doi.org/10.1016/j.pecs.2015.07.001

6. H.A. Michelsen, F. Liu, B.F. Kock, H. Bladh, A. Boiarciuc, M. Charwath et al., Modeling laser-induced incandescence of soot: a summary and comparison of LII models. Appl. Phys. B Lasers Opt. **87**, 503–521 (2007). https://doi.org/10.1007/s00340-007-2619-5

7. J. Reimann, S.A. Kuhlmann, S. Will, 2D aggregate sizing by combining laser-induced incandescence (LII) and elastic light scattering (ELS). Appl. Phys. B **96**, 583–592 (2009). https://doi.org/10.1007/s00340-009-3546-4

8. L.A. Melton, Soot diagnostics based on laser heating. Appl. Opt. **23**, 2201 (1984). https://doi.org/10.1364/AO.23.002201

9. A.C. Eckbreth, Effects of laser-modulated particulate incandescence on Raman scattering diagnostics. J. Appl. Phys. **48**, 4473–4479 (1977). https://doi.org/10.1063/1.323458

10. R.L. Vander Wal, T.M. Ticich, J.R. West, Laser-induced incandescence applied to metal nanostructures. Appl. Opt. **38**, 5867–5879 (1999). https://doi.org/10.1364/AO.38.005867

11. T.A. Sipkens, N.R. Singh, K.J. Daun, Time-resolved laser-induced incandescence characterization of metal nanoparticles. Appl. Phys. B Lasers **123**, 14 (2017). https://doi.org/10.1007/s00340-016-6593-7

12. T.A. Sipkens, N.R. Singh, K.J. Daun, N. Bizmark, M. Ioannidis, Examination of the thermal accommodation coefficient used in the sizing of iron nanoparticles by time-resolved laser-induced incandescence. Appl. Phys. B Lasers Opt. **119**, 561–575 (2015). https://doi.org/10.1007/s00340-015-6022-3

13. T.A. Sipkens, R. Mansmann, K.J. Daun, N. Petermann, J.T. Titantah, M. Karttunen et al., In situ nanoparticle size measurements of gas-borne silicon nanoparticles by time-resolved laser-induced incandescence. Appl. Phys. B Lasers Opt. **116**, 623–636 (2014). https://doi.org/10.1007/s00340-013-5745-2

14. J. Menser, K. Daun, T. Dreier, C. Schulz, Laser-induced incandescence from laser-heated silicon nanoparticles. Appl. Phys. B **122**, 277 (2016). https://doi.org/10.1007/s00340-016-6551-4

15. E.V. Gurentsov, A.V. Eremin, Size measurement of carbon and iron nanoparticles by laser induced incadescence. High Temp. **49**, 667–673 (2011). https://doi.org/10.1134/S0018151X11050087

16. A. Eremin, E. Gurentsov, E. Popova, K. Priemchenko, Size dependence of complex refractive index function of growing nanoparticles. Appl. Phys. B Lasers Opt. **104**, 285–295 (2011). https://doi.org/10.1007/s00340-011-4420-8

17. B.F. Kock, C. Kayan, J. Knipping, H.R. Orthner, P. Roth, Comparison of LII and TEM sizing during synthesis of iron particle chains. Proc. Combust. Inst. **30**, 1689–1696 (2005). https://doi.org/10.1016/j.proci.2004.07.034

18. B. Tribalet, A. Faccinetto, T. Dreier, C. Schulz, Evaluation of particle sizes of iron-oxide nano-particles in a low-pressure flame-synthesis reactor by simultaneous application of TiRe-LII and PMS. in 5th Int. Work. Laser-Induced Incandescence (2012)

19. S. Maffi, F. Cignoli, C. Bellomunno, S. De Iuliis, G. Zizak, Spectral effects in laser induced incandescence application to flame-made titania nanoparticles. Spectrochim. Acta Part B At. Spectrosc. **63**, 202–209 (2008). https://doi.org/10.1016/j.sab.2007.11.022

20. C. Schulz, B.F. Kock, M. Hofmann, H. Michelsen, S. Will, B. Bougie et al., Laser-induced incandescence: recent trends and current questions. Appl. Phys. B **83**, 333–354 (2006). https://doi.org/10.1007/s00340-006-2260-8

21. K.J. Daun, G.J. Smallwood, F. Liu, Investigation of thermal accommodation coefficients in time-resolved laser-induced incandescence. J. Heat Transf. **130**, 121201 (2008). https://doi.org/10.1115/1.2977549

22. D.R. Snelling, K.A. Thomson, F. Liu, G.J. Smallwood, Comparison of LII derived soot temperature measurements with LII model predictions for soot in a laminar diffusion flame. Appl. Phys. B Lasers Opt. **96**, 657–669 (2009). https://doi.org/10.1007/s00340-009-3614-9

23. M. Saffaripour, K.P. Geigle, D.R. Snelling, G.J. Smallwood, K.A. Thomson, Influence of rapid laser heating on the optical properties of in-flame soot. Appl. Phys. B Lasers Opt. **119**, 621–642 (2015). https://doi.org/10.1007/s00340-015-6072-6

24. G. Xiong, S. Li, Y. Zhang, S.G. Buckley, S.D. Tse, Phase-selective laser-induced breakdown spectroscopy of metal-oxide nanoparticle aerosols with secondary resonant excitation during flame synthesis. J. Anal. At. Spectrom. **31**, 482–491 (2016). https://doi.org/10.1039/C5JA00186B

25. Y. Zhang, G. Xiong, S. Li, Z. Dong, S.G. Buckley, S.D. Tse, Novel low-intensity phase-selective laser-induced breakdown spectroscopy of TiO_2 nanoparticle aerosols during flame

synthesis. Combust. Flame **160**, 725–733 (2013). https://doi.org/10.1016/j.combustflame.2012.11.007

26. J. Menser, K. Daun, T. Dreier, C. Schulz, Laser-induced atomic emission of silicon nanoparticles during laser-induced heating. Appl. Opt. **56**, 50–57 (2017)

27. C.F. Bohren, D.R. Huffman, Absorption and Scattering of Light by Small Particles. (Wiley, Germany, 1983)

28. T. Holstein, Optical and infrared volume absorptivity of metals. Phys. Rev. **96**, 535–536 (1954). https://doi.org/10.1103/PhysRev.96.535

29. H.A. Michelsen, M.A. Linne, B.F. Kock, M. Hofmann, B. Tribalet, C. Schulz, Modeling laser-induced incandescence of soot: enthalpy changes during sublimation, conduction, and oxidation. Appl. Phys. B Lasers Opt. **93**, 645–656 (2008). https://doi.org/10.1007/s00340-008-3181-5

30. H. Pan, J.A. Ritter, P.B. Balbuena, Examination of the approximations used in determining the isosteric heat of adsorption from the Clausius–Clapeyron equation. Langmuir **14**, 6323–6327 (1998). https://doi.org/10.1021/la9803373

31. C. Clavero, Plasmon-induced hot-electron generation at nanoparticle/metal-oxide interfaces for photovoltaic and photocatalytic devices. Nat. Photonics **8**, 95–103 (2014). https://doi.org/10.1038/nphoton.2013.238

32. M.J. Dresser, The Saha–Langmuir equation and its application. J. Appl. Phys. **39**, 338–339 (1968). https://doi.org/10.1063/1.1655755

33. R. Yen, J. Liu, N. Gloembergen, Thermally assisted multiphoton photoelectric emission from tungsten. Opt. Commun. **35**, 277–282 (1980). https://doi.org/10.1016/0030-4018(80)90228-X

34. S.L. Chin. *Multiphoton Ionization of Atoms*. (Elsevier Science, New York, 1984)

35. A.W. Miziolek, V. Palleschi, I. Schechter, *LIBS Fundamentals and Applications*. (Cambridge University Press, Cambridge, 2006). https://doi.org/10.1017/CBO9780511541261

36. T.L.F. Leung, H.M. Van Driel, Time-resolved thermionic and photoemission from nanosecond, pulsed laser excited germanium and silicon. Appl. Phys. Lett. **45**, 683–685 (1984). https://doi.org/10.1063/1.95356

37. C.G. Found, Ionization potentials of argon, nitrogen, carbon monoxide, helium, hydrogen and mercury and iodine vapors. Phys. Rev. **16**, 41–53 (1920). https://doi.org/10.1103/PhysRev.16.41

38. A.G. Chynoweth, Ionization rates for electrons and holes in silicon. Phys. Rev. **109**, 1537–1540 (1958). https://doi.org/10.1103/PhysRev.109.1537

39. S. Maier, *Plasmonics: Fundamentals and Applications* (Springer, US, 2007)

40. S. Talebi Moghaddam, H. Ertürk, M.P. Mengüç, Enhancing local absorption within a gold nano-sphere on a dielectric surface under an AFM probe. J. Quant. Spectrosc. Radiat. Transf. (2016). https://doi.org/10.1016/j.jqsrt.2016.02.011

41. G. Bisker, D. Yelin, Noble-metal nanoparticles and short pulses for nanomanipulations: theoretical analysis. J. Opt. Soc. Am. B **29**, 1383–1383 (2012). https://doi.org/10.1364/JOSAB.29.001383

42. A. Hatef, M. Meunier, Plasma-mediated photothermal effects in ultrafast laser irradiation of gold nanoparticle dimers in water. Opt. Express **23**, 1967 (2015). https://doi.org/10.1364/OE.23.001967

43. J. Schäfer, S.C. Lee, A. Kienle, Calculation of the near fields for the scattering of electromagnetic waves by multiple infinite cylinders at perpendicular incidence. J. Quant. Spectrosc. Radiat. Transf. **113**, 2113–2123 (2012). https://doi.org/10.1016/j.jqsrt.2012.05.019

44. H. Suzuki, I.S. Lee, Calculation of the Mie scattering field inside and outside a coated spherical particle. Int. J. **3**, 38–41 (2008)

45. C. Sönnichsen, T. Franzl, T. Wilk, G. von Plessen, J. Feldmann, O. Wilson et al., Drastic reduction of plasmon damping in gold nanorods. Phys. Rev. Lett. **88**, 077402 (2002). https://doi.org/10.1103/PhysRevLett.88.077402

46. J. Hofmann, W. Steinmann, Plasma Resonance in the Photoemission of Silver. Phys. Status Solidi **30**, K53–K56 (1968). https://doi.org/10.1002/pssb.19680300160

47. J.G. Endriz, W.E. Spicer, Surface-plasmon-one-electron decay and its observation in photoemission. Phys. Rev. Lett. **24**, 64–68 (1970). https://doi.org/10.1103/PhysRevLett.24.64

48. T. Inagaki, K. Kagami, E.T. Arakawa, Photoacoustic observation of nonradiative decay of surface plasmons in silver. Phys. Rev. B **24**, 3644–3646 (1981). https://doi.org/10.1103/PhysRevB.24.3644

49. A.V. Uskov, I.E. Protsenko, R.S. Ikhsanov, V.E. Babicheva, S.V. Zhukovsky, A.V. Lavrinenko et al., Internal photoemission from plasmonic nanoparticles: comparison between surface and volume photoelectric effects. Nanoscale **6**, 4716–4727 (2014). https://doi.org/10.1039/c3nr06679g

50. M.W. Knight, Y. Wang, A. Urban, A. Sobhani, B. Zheng, P. Nordlander et al., Embedding plasmonic nanostructure-diodes enhances hot electron emission. Nano Lett. **13**, 1687–1692 (2013). https://doi.org/10.1021/nl400196z

51. C. Ropers, T. Elsaesser, G. Cerullo, M. Zavelani-Rossi, C. Lienau. Ultrafast optical excitations of metallic nanostructures: from light confinement to a novel electron source. New J. Phys. (2007). https://doi.org/10.1088/1367-2630/9/10/397

52. A.V. Filippov, M.W. Markus, P. Roth, In-situ characterization, of ultrafine particles by laser-induced incandescence, sizing and particle structure determination. J. Aerosol Sci. **30**, 71–87 (1999)

53. J.P. Perdew, Energetics of charged metallic particles: from atom to bulk solid. Phys. Rev. B **37**, 6175–6180 (1988). https://doi.org/10.1103/PhysRevB.37.6175

54. L. Landström, P. Heszler, Analysis of blackbody-like radiation from laser-heated gas-phase tungsten nanoparticles. J. Phys. Chem. B **108**, 6216–6221 (2004). https://doi.org/10.1021/jp0367629

55. J.M. Mitrani, M.N. Shneider, B.C. Stratton, Y. Raitses, Modeling thermionic emission from laser-heated nanoparticles. Appl. Phys. Lett. **108**, 054101 (2016). https://doi.org/10.1063/1.4940992

56. A. Kramida, Y. Ralchenko, J. Reader, and NIST ASD Team. NIST Atomic Spectra Database (version 5.2). National Institute of Standards and Technology (2015). http://physics.nist.gov/asd

57. V.G. Sevast'yanov, P.Y. Nosatenko, V.V. Gorskii, Y.S. Ezhov, D.V. Sevast'yanov, E.P. Simonenko et al., Experimental and theoretical determination of the saturation vapor pressure of silicon in a wide range of temperatures. Russ. J. Inorg. Chem. **55**, 2073–2088 (2010). https://doi.org/10.1134/S0036023610130036

58. J.H. Bechtel, W. Lee Smith, N. Bloembergen, Two-photon photoemission from metals induced by picosecond laser pulses. Phys. Rev. B **15**, 4557–4563 (1977). https://doi.org/10.1103/PhysRevB.15.4557

59. A.M. Malvezzi, H. Kurz, N. Bloembergen, Nonlinear photoemission from picosecond irradiated silicon. Appl. Phys. A Solids Surf. **36**, 143–146 (1985). https://doi.org/10.1007/BF00624934

60. R.P. Brogle, Studies of linear and nonlinear photoemission processes in metals and semiconductors. University of California, 1996

61. P.B. Jackson, *Numerical Modeling of the Plasma-Particle Interactions of Aerosol Vaporization in a Laser-Induced Plasma*. University of Florida, 2011

62. J.C. Carls, J.R. Brock, Propagation of laser breakdown and detonation waves in transparent droplets. Opt. Lett. **13**, 273–275 (1988). https://doi.org/10.1364/OL.13.000273

63. P.K. Diwakar, D.W. Hahn, Study of early laser-induced plasma dynamics: transient electron density gradients via Thomson scattering and Stark Broadening, and the implications on laser-induced

breakdown spectroscopy measurements. Spectrochim. Acta Part B **63**, 1038–1046 (2008). https://doi.org/10.1016/j.sab.2008.07.003

64. J.L. Beduneau, Y. Ikeda, Spatial characterization of laser-induced sparks in air. J. Quant. Spectrosc. Radiat. Transf. **84**, 123–139 (2004). https://doi.org/10.1016/S0022-4073(03)00136-5

65. Y. Oh, R. Zahaf, M.R. Zachariah, D. Lee, Nanosecond laser induced energetic ion formation from a nanoparticle: the origin of ion detection loss in a single particle mass spectrometry. Jpn. J. Appl. Phys. **53**, 05HA10 (2014)

66. P.K. Diwakar, *Laser-Induced Plasmas as an Analytical Source for Quantitative Analysis of Gaseous and Aerosol Systems: Fundamentals of Plasma-Particle Interactions*. University of Florida, 2009

67. W. Lochte-Holtgreven. *Plasma Diagnostics*. (AIP Press, Collage Park, 1995)

68. G.B. Rybicki, A.P. Lightman. *Radiative Processes in Astrophysics*. (Wiley, Hoboken, 2008)

69. A.N. Cox. *Allen's Astrophysical Quantities*. (Springer, New York, 2015)

70. R.R. Johnston, Free-free radiative transitions-a of theoretical results. J. Quant. Spectrosc. Radiat. Transf. **7**, 815–835 (1967)

71. J. Park, I. Henins, H.W. Herrmann, G.S. Selwyn, Neutral bremsstrahlung measurement in an atmospheric-pressure radio frequency discharge. Phys. Plasmas **7**, 3141–3144 (2000). https://doi.org/10.1063/1.874220

72. T. Ohmura, H. Ohmura, Continuous absorption due to free-free transitions in hydrogen. Phys. Rev. **121**, 513–517 (1961). https://doi.org/10.1103/PhysRev.121.513

73. Y. Itikawa, Momentum-transfer cross sections for electron collisions with atoms and molecules. At. Data Nucl. Data Tables **14**, 1–10 (1974). https://doi.org/10.1016/S0092-640X(74)80026-4

74. L.J. Radziemski, D.A. Cremers. *Laser-Induced Plasmas and Applications*. (M. Dekker, New York, 1989)

75. F. Memarian, K.J. Daun, Gas Dynamics of Sublimed Nanoclusters in High-Fluence Time-Resolved Laser-Induced Incandescence. Numer. Heat Transf. Part B Fundam. **65**, 393 (2014). https://doi.org/10.1080/10407790.2013.869098

76. F. Memarian, F. Liu, K.A. Thomson, K.J. Daun, D.R. Snelling, G.J. Smallwood, Effect of recondensation of sublimed species on nanoparticle temperature evolution in time-resolved laser-induced incandescence. Appl. Phys. B Lasers Opt. **119**, 607–620 (2015). https://doi.org/10.1007/s00340-015-6077-1

77. S. Krishnan, K.J. Yugawa, P.C. Nordine, Optical properties of liquid nickel and iron. Phys. Rev. B **55**, 8201 (1997). https://doi.org/10.1103/PhysRevB.55.8201

78. B.T. Barnes, Optical Constants of incandescent refractory metals. J. Opt. Soc. Am. **56**, 1546 (1966). https://doi.org/10.1364/JOSA.56.001546

79. R.L. Taylor, G. Caledonia, Experimental determination of the cross-sections for neutral bremsstrahlung I. Ne, Ar and Xe. J. Quant. Spectrosc. Radiat. Transf. **9**, 657–679 (1969). https://doi.org/10.1016/0022-4073(69)90014-4

80. R.T.V. Kung, C.H. Changs, Neutral bremsstrahlung radiation of Ne, Ar and O. J. Quant. Spectrosc. Radiat. Transf. **16**, 579 (1976). https://doi.org/10.1016/0022-4073(76)90024-8

81. R.L. Vander Wal, M.Y. Choi, K. Lee, The effects of rapid heating of soot: implications when using laser-induced incandescence for soot diagnostics. Combust. Flame **102**, 200–204 (1995). https://doi.org/10.1016/0010-2180(95)00071-D

82. H. Bladh, P.E. Bengtsson, Characteristics of laser-induced incandescence from soot in studies of a time-dependent heat- and mass-transfer model. Appl. Phys. B Lasers Opt. **78**, 241–248 (2004). https://doi.org/10.1007/s00340-003-1362-9